<Society logo(s) and publication title will appear here.>

Received XX Month, XXXX; revised XX Month, XXXX; accepted XX Month, XXXX; Date of publication XX Month, XXXX; date of current version XX Month, XXXX.

Digital Object Identifier 10.1109/XXXX.2022.1234567

Wireless Power and Data Transfer for Robotic Joints Using High Coupling Magnetic Cores and Photodiode-Based Communication

David Sirianni[1], Takanobu Ohno[1], Member, IEEE, and Spasoje Mirić[1], Member, IEEE

[1]Institute for Mechatronics, University of Innsbruck, Technikerstr. 13a, 6020 Innsbruck, Austria

Corresponding author: Spasoje Mirić (e-mail: spasoje.miric@uibk.ac.at)

The authors gratefully acknowledge the financial support provided by UIBK's 1669 Prototypenentwicklung funding for this project.

ABSTRACT Robotic systems, such as legged robots or industrial robots used in manufacturing and humanoid assistance, rely on robotic joints to perform multi-degree-of-freedom motions. Each joint typically incorporates a motor and a gear to drive its motion. Power delivery and control for these joints are usually achieved through cables for power and data transfer, which are routed through the joints. However, as the joints move, these cables bend and flex, leading to eventual failure due to the limited number of bending cycles they can withstand. Additionally, in high-precision joints, cable slack can disrupt position control accuracy. To address these challenges, this paper investigates wireless power and data transfer (WPDT) for robotic joints. The proposed approach leverages a closed magnetic core for power transfer, minimizing stray magnetic fields, and uses photodiode-based communication with a custom-developed control circuit. The approach is validated through experimental measurements and benchmarked against existing solutions in the literature. We demonstrate a system capable of transferring 200 W of power and achieving a data transfer rate of 2 Mbit/s, with the total weight of all components being 96 gram.

INDEX TERMS Wireless Data Transfer, Wireless Power Transfer, Robotic Joint

I. INTRODUCTION

ROBOTIC systems, particularly legged robots, are increasingly employed in demanding industrial environments where they must traverse various obstacles, such as climbing stairs. These robots are typically designed with four legs, as this configuration allows them to navigate and overcome challenging terrains more effectively. Each robotic leg typically features three joints: two in the shoulder and one in the knee, as described in [1].

Each joint typically comprises a motor paired with a gearbox, achieving gear ratios typically ranging from 6:1 to 200:1. To achieve smooth and coordinated motion of the 4-leg robot, the legs must operate under synchronized motion control. This synchronization is managed by a central control unit, which handles higher-level control tasks and generates precise position references for each motor in every joint. To transmit position reference data to each motor joint, a data connection is established between the central control unit and each robot joint. Additionally, power is distributed from a battery, typically located at the center of the robot's body, to each joint [2].

To establish the connection between the legs and the central body of the robot (for both data and power), current robotic systems rely on cables. However, to connect to joints that are second or third in a sequence—such as the second shoulder joint and the knee joint—the cables must pass through preceding joints. For instance, cables for the knee joint must first pass through both shoulder joints. These cables, which traverse through the joints, are subjected to bending and twisting motions as the joints operate. Over time, this leads to mechanical failure due to the limited number of bending cycles the cables can endure, thereby reducing their operational lifetime [3], [4].

This work is licensed under a Creative Commons Attribution 4.0 License. For more information, see https://creativecommons.org/licenses/by/4.0/

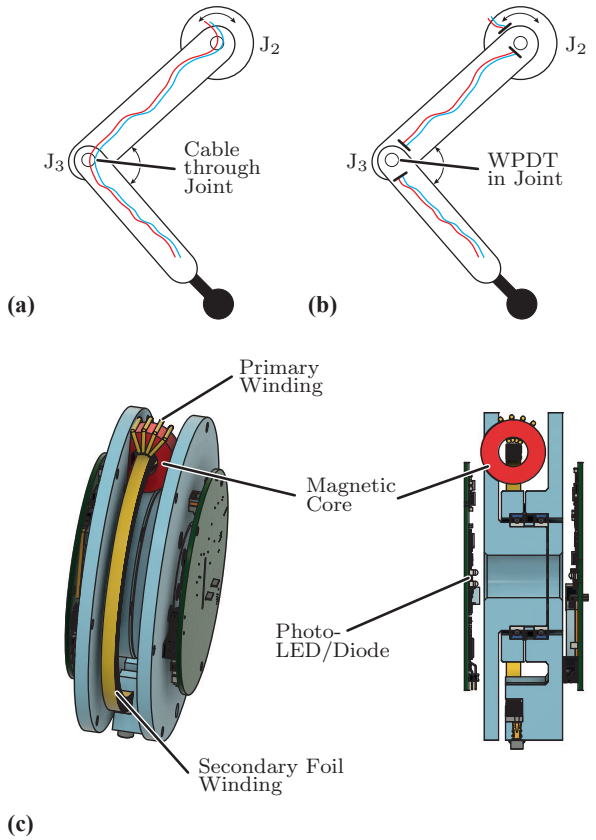

FIGURE 1: Typical joint arrangements in a robotic leg: (a) A robotic leg with wired data and power transmission, where cables pass through the joint. (b) Wire routing in a WPDT system, eliminating the need for cables to pass through the joints. (c) The concept of the proposed WPDT approach.

This challenge can be addressed by introducing wireless power and data transfer (WPDT) in robotic joints, as shown in systems like [3]–[6]. Although this approach increases the complexity of the robotic leg, it eliminates the need for moving cables, which significantly improves the reliability and longevity of the joints. Figure 1(a) illustrates how cables must pass through joint J2 to reach joint J3. Consequently, any movement of J2 causes bending and twisting of the cables. In contrast, Figure 1(b) demonstrates the conceptual implementation of the WPDT approach, where cables do not bend, eliminating the risk of mechanical failure.

The majority of the literature, such as [3]–[6], relies on inductive coupling for power transfer, which typically involves an air gap between the primary and secondary windings. This results in unavoidable stray fields that can affect nearby components within the joint. To address these challenges, this paper proposes a closed-core-based wireless power transfer (WPT) system, as depicted in Fig. 2. The approach employs a closed nanocrystalline toroidal core for inductive coupling between the primary and secondary windings. As shown in [7], a similar closed-core approach has been successfully used for wireless power transfer to a linear actuator enclosed in stainless steel, where the stainless steel had a negligible impact on power transfer efficiency since the coupling field is focused inside the closed core, which significantly reduces stray fields. Therefore, this design minimizes the risk of induced eddy current losses in nearby conductive structural components and also lowers the potential for field radiation originating from those eddy currents. It should be noted, however, that precise EMI radiation levels were not analyzed. This aspect will be addressed in future work, as currents from the secondary coils can still contribute to EMI. Consequently, compliance with relevant electromagnetic compatibility (EMC) standards and guidelines for limiting exposure to time-varying electric, magnetic, and electromagnetic fields will need to be carefully evaluated.

The practical design of this WPT system leaves the central space of the joint free, which is utilized for wireless data transfer. For this purpose, infrared photodiodes and LED's are placed precisely in the middle of the leg, close to the central joint axis. This alignment ensures that the diodes remain properly positioned during joint rotation, enabling continuous communication. Visible light-based data transmission, similar to the proposed approach, has been reported in the literature [8], achieving data speeds of up to $200\,\mathrm{kbit\,s^{-1}}$. In this paper, we demonstrate simultaneous wireless power and data transmission (WPT and WDT) with power levels up to $200\,\mathrm{W}$ and data transmission speeds reaching $2\,\mathrm{Mbit\,s^{-1}}$.

In Sec. II, we discuss the principles of wireless power transfer and provide a detailed overview of the WPT model, including loss models for the windings and the magnetic core. This model is then utilized for optimization to determine the optimal system parameters. The concept of wireless data transmission is introduced in Sec. III, where we present a comprehensive overview of the data transmission circuit. Finally, Sec. IV covers the hardware implementation and experimental results, demonstrating the successful operation of the prototype.

II. Wireless Power Transfer: Principle and Design

For wireless power transfer (WPT) in rotational joints, two parallel or axially arranged coils combined with magnetic materials are commonly employed. In some cases, multiple parallel coils have also been explored [9]. However, these WPT approaches typically involve a magnetic air gap between the coils, which reduces the magnetic coupling in the system. In this work, we utilize a closed magnetic core to maximize the magnetic coupling. The functioning principle of this approach is explained in the following.

A. WPT Principle

The WPT system of the joint consists of two windings and a toroidal core for magnetic coupling, as depicted in Fig. 2(a). The primary winding is wound around the toroidal

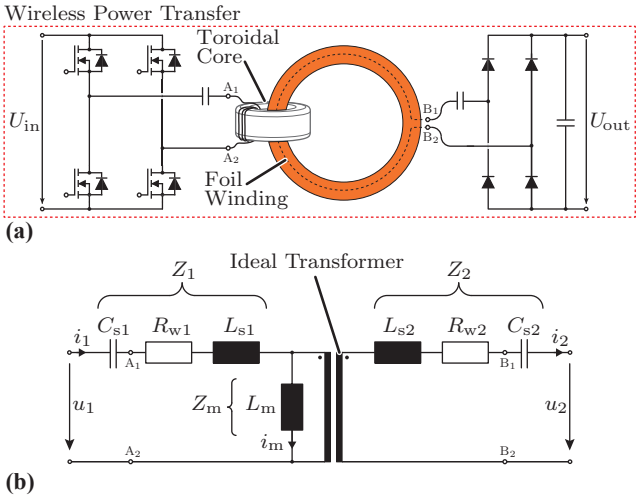

FIGURE 2: Overview of the proposed wireless power transfer for robotic joints: (a) The conceptual schematic of the system with the closed magnetic core. (b) Equivalent circuit of the WPT with series resonant compensation.

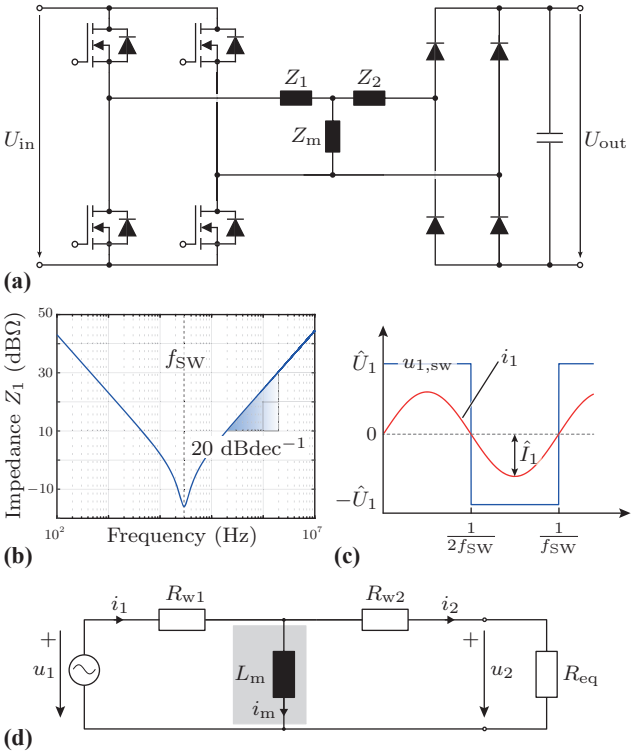

FIGURE 3: Equivalent circuit and waveforms of the DC-DC converter: (a) Schematic of the equivalent circuit. (b) The amplitude of Z_1 over the frequency is shown. (c) Primary side voltage and current waveforms, showing so-called DC transformer operation [10]. (d) Equivalent circuit after resonant compensation.

core, and the core, together with the primary winding, can rotate around the secondary winding. The secondary winding, referred to as the foil winding, is constructed using copper foil, with further details provided later in this section.

This assembly of the core and windings can be modeled using a transformer T-equivalent circuit, as shown in Fig. 2(b). The winding resistance of the primary side is represented by R_{w1}, while that of the secondary side is represented by R_{w2}. The stray inductances of the primary and secondary windings are denoted as L_{s1} and L_{s2}, respectively. In this configuration, it is expected that $L_{s1} \ll L_{s2}$, as the primary winding is tightly wound around the core. The magnetization inductance is represented by L_m, which can be directly calculated from the A_L value provided in the datasheets of the toroidal core.

The ideal transformer in the circuit represents the turns ratio of the windings. However, since this WPT system is designed to maintain equal voltage levels for the primary and secondary windings, both windings have the same number of turns. This results in an ideal transformer turns ratio of 1:1, which can be neglected in further analysis for simplicity.

A limitation of the proposed approach is that it cannot achieve full 360° rotation around the joint axis. This is due to the mechanical fixation point and electrical connection of the foil winding, around which the core rotates within the joint. Consequently, the rotation angle is restricted by the size of the core and the connection of the foil winding, as illustrated in Fig. 4. In this setup, the achievable rotation angle is approximately $\alpha = 310°$. However, this limitation does not present a disadvantage for joints used in robotic legs, as such joints typically do not require continuous 360° rotation. According to [1], a rotation angle α of 270° is sufficient to achieve even complex motion sequences.

B. WPT Model

1) Resonant Compensation

Due to the geometry of the secondary coil (denoted as the foil winding in Fig. 4), it cannot be tightly wound around the core to allow for relative rotation between the primary and secondary windings. As a result, the system exhibits leakage inductance, which, at the operating frequency of the WPT—typically in the kilohertz range—cannot be neglected and may cause significant voltage drops.

To mitigate this issue, resonant compensation with series capacitors, as shown in Fig. 2(b), are employed [11]. Various types of resonant compensation methods have been studied in the literature [12]. However, due to its simpler implementation and its voltage source behavior at the output [13], the series-series resonant compensation method is used. In this approach, capacitors C_{s1} and C_{s2} are connected in series with the leakage inductances L_{s1} and L_{s2}, respectively.

The values of the capacitors are chosen such that, at the switching frequency f_{SW}, the impedance of the capacitors

cancels out the impedance of the corresponding stray inductances. This is achieved by selecting the capacitor values as follows:

$$C_{\mathrm{s1}} = \frac{1}{\left(2\pi f_{\mathrm{SW}}\right)^2 L_{\mathrm{s1}}}, \quad C_{\mathrm{s2}} = \frac{1}{\left(2\pi f_{\mathrm{SW}}\right)^2 L_{\mathrm{s2}}}. \tag{1}$$

This ensures that the impedance of the capacitors and the stray inductances at the switching frequency is reduced to zero, eliminating the voltage drop across these components. Consequently, the impact of the stray inductance on the WPT system is effectively negated.

2) Fundamental Frequency Equivalent Circuit

The primary and secondary windings of the analyzed WPT system (see Fig. 2(a)) are supplied by a full-bridge converter on the primary side and a rectifier circuit on the secondary side, as depicted in Fig. 3(a). The impedances Z_1, Z_2, and Z_{m} represent series connection of elements shown in Fig. 2(b). The resonant capacitors C_{s1} and C_{s2}, tuned according to (1), ensure that the stray inductances cancel out at the switching frequency f_{SW} of the full-bridge converter. As shown in Fig. 3(b), this results in the impedance exhibiting capacitive behavior for frequencies lower than f_{SW} and inductive behavior for frequencies higher than f_{SW}, [11]. Consequently, the impedance Z_1 increases significantly for frequencies other than f_{SW}.

This behavior causes the currents in the system to remain almost sinusoidal, as illustrated in Fig. 3(c). Even though the voltage waveform from the full-bridge converter is square-shaped and contains higher-order harmonics beyond the fundamental switching frequency, the current in the WPT system remains sinusoidal. This is because the higher voltage harmonics are effectively filtered out by the impedances Z_1 and Z_2.

Therefore, these systems are modeled at the fundamental frequency. Specifically, the input square wave voltage is given by $u_{1,\mathrm{sw}} = U_{\mathrm{in}} \cdot \mathrm{sgn}(\sin(2\pi f_{\mathrm{sw}} t))$, where sgn is the sign function, which equals -1 if its argument is negative and 1 if its argument is positive. This square wave voltage can be replaced with an equivalent sinusoidal voltage: $u_1 = \hat{U}_1 \sin(2\pi f_{\mathrm{sw}} t)$, where $\hat{U}_1 = \frac{4}{\pi} U_{\mathrm{in}}$ represents the amplitude of the first harmonic in the Fourier series of $u_{1,\mathrm{sw}}$.

To verify this equivalence, consider the active power calculated using the square wave voltage:

$$P_1 = U_{\mathrm{in}} \cdot \frac{1}{T_{\mathrm{sw}}/2} \int_0^{T_{\mathrm{sw}}/2} \hat{I}_1 \sin(2\pi f_{\mathrm{sw}} t)\, \mathrm{d}t = U_{\mathrm{in}} \cdot \frac{2}{\pi} \hat{I}_1. \tag{2}$$

This must be equal to the active power calculated using the equivalent sinusoidal voltage:

$$P_1 = \frac{1}{2} \hat{U}_1 \hat{I}_1. \tag{3}$$

Equating these expressions shows that:

$$\hat{U}_1 = \frac{4}{\pi} U_{\mathrm{in}}. \tag{4}$$

Similarly, for the secondary side, the fundamental frequency voltage amplitude is related to the output voltage by:

$$\hat{U}_2 = \frac{4}{\pi} U_{\mathrm{out}}. \tag{5}$$

The fundamental frequency equivalent circuit is depicted in Fig. 3(d), where the stray inductances L_{s1} and L_{s2}, as well as the resonant capacitors C_{s1} and C_{s2}, are absent as they cancel each other at the switching frequency f_{SW}. To estimate the currents in this circuit, an equivalent resistor R_{eq} is introduced to model the active power P_2 drawn from the secondary side. The power dissipated on this equivalent resistor is calculated as

$$P_2 = \frac{1}{2} \frac{\hat{U}_2^2}{R_{\mathrm{eq}}}. \tag{6}$$

Substituting $\hat{U}_2$ from (5), we obtain

$$P_2 = \frac{1}{2} \frac{16}{\pi^2} U_{\mathrm{out}}^2 \frac{1}{R_{\mathrm{eq}}}, \tag{7}$$

which allows us to express the equivalent resistance as

$$R_{\mathrm{eq}} = \frac{8}{\pi^2} \frac{U_{\mathrm{out}}^2}{P_2}. \tag{8}$$

Here, U_{out} denotes the DC output voltage, and P_2 represents the delivered output power. In practical implementations, the equivalent load resistance R_{eq} is defined by the application context. Specifically, in motor drive systems, the required output power is largely determined by the mechanical load acting on the motor. The modeling approach employed enables the specification of a target output power P_2 by appropriately selecting R_{eq} in accordance with (8). It is important to emphasize that this equivalent load modeling is valid only under the assumption of constant DC output voltage and current, which presumes the presence of sufficiently robust output filtering. In practical WPT system configurations, the DC output is typically interfaced with a DC bus that includes strong filtering stages, thereby justifying the assumption of idealized DC output conditions.

C. WPT Losses

1) Winding Losses

The established fundamental frequency model of the WPT, as shown in Fig. 3(d), is used to calculate the winding losses. In this WPT system, a closed nanocrystalline core with high permeability is employed, resulting in a high magnetization inductance L_{m}. This allows the magnetization current to be approximated as negligible, $i_{\mathrm{m}} \approx 0$, leading to $i_1 \approx i_2$. Consequently, the currents can be expressed as:

$$\hat{I}_1 = \hat{I}_2 = \frac{\hat{U}_1}{R_{\mathrm{w1}} + R_{\mathrm{w2}} + R_{\mathrm{eq}}}.$$

Where $\hat{U}_1$ is given in (4). The primary winding losses are then calculated as

$$P_{\mathrm{w1}} = \frac{1}{2} R_{\mathrm{w1}} \hat{I}_1^2, \tag{9}$$

and the winding losses of the secondary are calculated as

$$P_{\mathrm{w2}} = \frac{1}{2} R_{\mathrm{w2}} \hat{I}_2^2. \tag{10}$$

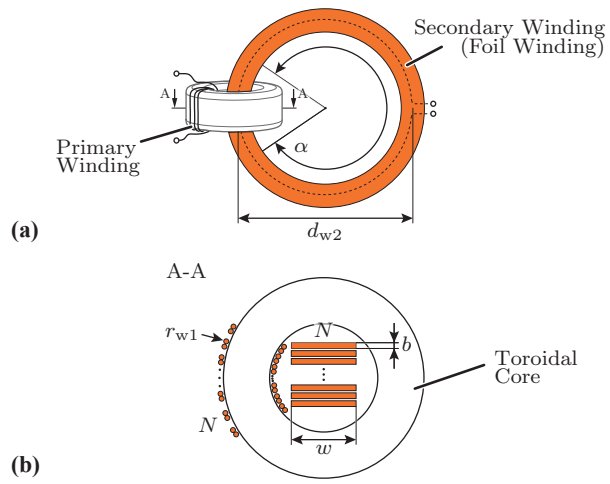

FIGURE 4: Geometric parameters of the presented WPT approach: (a) The range of rotation α of the joint, limited by the size of the core and the connection point of the foil winding. (b) Cross-section A-A through the core and windings.

TABLE 1: Steinmetz parameter for Vitroperm 500F

Steinmetz Parameter	α	β	k_i
Value	1.88	2.02	$137 \cdot 10^{-6}$

2) Core Losses

Modeling core losses is a challenging task and has been extensively studied by many researchers. One of the most widely used methods is the Steinmetz equation. However, since this equation applies only to sinusoidal magnetic flux, and in our case, the squared voltage results in triangular flux, the improved Generalized Steinmetz Equation (GSE) is utilized [14] for the core loss density ($\mathrm{W\,m^{-3}}$)

$$p_{\mathrm{core}} = \frac{1}{T}\int_0^T k_i \left|\frac{\mathrm{d}B}{\mathrm{d}t}\right|^{\alpha} (\Delta B)^{\beta-\alpha}\,\mathrm{d}t, \tag{11}$$

where $\frac{\mathrm{d}B}{\mathrm{d}t}$ represents the rate of change of the magnetic flux density, ΔB denotes the peak-to-peak flux density, and T is the period duration, as shown in Fig. 5. The parameter k_i is given by:

$$k_i = \frac{k}{(2\pi)^{\alpha-1}\int_0^{2\pi} |\cos\theta|^{\alpha}\, 2^{\beta-\alpha}\mathrm{d}\theta}.$$

The values for the parameters k, α, and β are empirically determined for magnetic materials. For the nanocrystalline material Vitroperm 500F used in this study, these values are listed in Tab. 1 and taken from [14].

Due to the pulsed voltage shape, the flux linkage, and consequently the flux density in the core, exhibit a triangular waveform, as illustrated in Fig. 5. As a result, the rate of change of the flux density $\frac{\mathrm{d}B}{\mathrm{d}t}$ in (11) can be expressed as a function of the input voltage:

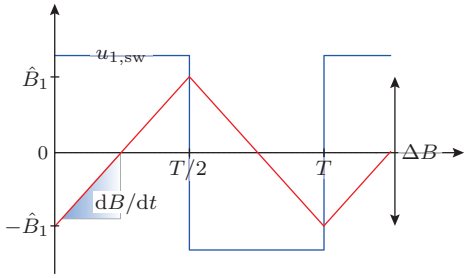

FIGURE 5: Triangular waveform of the flux density B, due to the rectangular voltage $u_{1,\mathrm{sw}}$.

$$\left|\frac{\mathrm{d}B}{\mathrm{d}t}\right| = \frac{U_{\mathrm{in}}}{NA_{\mathrm{Fe}}}, \tag{12}$$

where A_{Fe} denotes the effective cross-sectional area of the magnetic core, N is the number of windings, and f_{SW} is the switching frequency of the full-bridge inverter. The peak value of the flux density $\hat{B}$ can be calculated as:

$$\hat{B} = \frac{\hat{\Psi}}{A_{\mathrm{Fe}}} = \frac{U_{\mathrm{in}}}{4NA_{\mathrm{Fe}}f_{\mathrm{SW}}}. \tag{13}$$

Substituting (12) and (13) into (11) results in the following core loss equation:

$$P_{\mathrm{core}} = k_i \left|\frac{U_{\mathrm{in}}}{NA_{\mathrm{Fe}}}\right|^{\alpha} \left(\frac{U_{\mathrm{in}}}{2NA_{\mathrm{Fe}}f_{\mathrm{SW}}}\right)^{\beta-\alpha} V_{\mathrm{core}}, \tag{14}$$

where V_{core} represents the volume of the magnetic core.

D. WPT Efficiency

The efficiency of the WPT system can be calculated using the input power and the combined winding and core losses as:

$$\eta = \frac{P_{\mathrm{in}} - P_{\mathrm{loss}}}{P_{\mathrm{in}}},$$

where the input power is determined as:

$$P_{\mathrm{in}} = \frac{1}{2}\hat{U}_1\hat{I}_1 = \frac{1}{2}\frac{\hat{U}_1^2}{R_{\mathrm{w1}} + R_{\mathrm{w2}} + R_{\mathrm{eq}}},$$

with $\hat{U}_1$ given in (4). The total losses are calculated as:

$$P_{\mathrm{loss}} = P_{\mathrm{w1}} + P_{\mathrm{w2}} + P_{\mathrm{core}},$$

where P_{w1} and P_{w2} represent the winding losses on the primary and secondary sides, respectively, and P_{core} accounts for the core losses.

E. Winding Resistance Model

To calculate the winding losses, it is first necessary to determine the winding resistance. This section establishes a model for winding resistance, which involves calculating the DC resistance and then accounting for its increase due to winding temperature rise and the impact of the operating frequency, known as AC resistance.

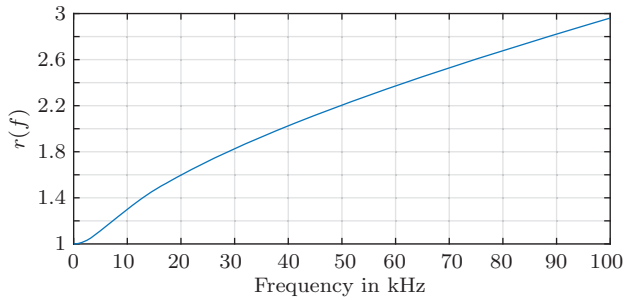

FIGURE 6: Simulated resistance change $r(f)$ over frequency for a foil winding with $N = 15$, $w = 5\,\mathrm{mm}$ and $b = 0.1\,\mathrm{mm}$.

The DC winding resistance is calculated using the geometrical parameters of the windings depicted in Fig. 4(b). The primary winding consists of two solid round wires with a radius r_{w1} connected in parallel, tightly wound around the toroidal core. Two wires are used in parallel to reduce r_{w1} and thereby minimize losses caused by the skin effect. A compact core is chosen to minimize volume, making it easier to fit into robotic joints. For this core, one turn of the winding has a length of $l_{\mathrm{w1}} = 4.4\,\mathrm{cm}$, resulting in the following expression for the DC winding resistance:

$$R_{\mathrm{dc1}} = \frac{1}{\sigma_{\mathrm{cu}}} \frac{N l_{\mathrm{w1}}}{2\pi r_{\mathrm{w1}}^2}.$$

Here, $\sigma_{\mathrm{cu}} = 58\,\mathrm{MS/m}$ is the conductivity of copper at an ambient temperature of $20\,^{\circ}\mathrm{C}$. A temperature correction for the winding resistance will be introduced later to account for temperature variations. The DC resistance of the secondary foil winding, based on the geometrical parameters shown in Fig. 4(b), is calculated as:

$$R_{\mathrm{dc2}} = \frac{1}{\sigma_{\mathrm{cu}}} \frac{N \pi d_{\mathrm{w2}}}{w \cdot b},$$

where d_{w2} is the average diameter of the secondary winding, and w and b are its width and thickness, respectively.

To calculate the final values of the winding resistances, we account for the effects of winding temperature and the frequency-dependent current distribution. The winding resistance is expressed as:

$$\begin{aligned} R_{\mathrm{w1}} &= R_{\mathrm{dc1}} \cdot (1 + \alpha_{\mathrm{cu}} \Delta T)\,, \\ R_{\mathrm{w2}} &= R_{\mathrm{dc2}} \cdot (1 + \alpha_{\mathrm{cu}} \Delta T) \cdot r(f), \end{aligned}$$

where $\alpha_{\mathrm{cu}} = 0.0039\,^{\circ}\mathrm{C}^{-1}$ is the copper temperature coefficient.

To determine the temperature increase in the windings and ensure that the temperature limits are not exceeded, the thermal resistances of the prototype windings were measured. Since the primary winding is close to the magnetic core, the temperature limit is defined by the maximum allowable core temperature, $T_{\mathrm{w1,max}} = T_{\mathrm{c,max}} = 60\,^{\circ}\mathrm{C}$, while the secondary winding's temperature limit is determined by the insulation temperature limit, $T_{\mathrm{w2,max}} = 190\,^{\circ}\mathrm{C}$. The thermal resistance of the primary winding was measured as $R_{\mathrm{th1}} = 24.3\,^{\circ}\mathrm{C\,W^{-1}}$, while the secondary winding exhibits a thermal resistance of $R_{\mathrm{th2}} = 10.4\,^{\circ}\mathrm{C\,W^{-1}}$. These values are used to iteratively estimate the winding temperatures, ensuring that they remain within the permissible limits:

$$\begin{aligned} &T_{\mathrm{amb}} + \frac{1}{2} R_{\mathrm{w1}} \hat{I}_1^2 \cdot R_{\mathrm{th1}} < T_{\mathrm{w1,max}}, \quad \text{(primary winding)}, \\ &T_{\mathrm{amb}} + \frac{1}{2} R_{\mathrm{w2}} \hat{I}_2^2 \cdot R_{\mathrm{th2}} < T_{\mathrm{w2,max}}, \quad \text{(secondary winding)}. \end{aligned} \tag{15}$$

The frequency dependence of the secondary winding resistance is determined using a FEM eddy current model of the windings in Ansys EM Suite [15]. The relative frequency dependence $r(f)$ is simulated for various configurations of the secondary winding. For instance, Fig. 6 illustrates $r(f)$ for $N = 15$, $w = 5\,\mathrm{mm}$, and $b = 0.1\,\mathrm{mm}$. It is worth noting that, due to the geometry of the primary winding (a single layer with each turn slightly displaced), the primary winding resistance exhibits no significant frequency dependence within the analyzed frequency range (up to $50\,\mathrm{kHz}$). Therefore, there is no need to use $r(f)$ for the primary winding.

F. Thermal Model of the Magnetic Core

In the analyzed WPT system, a nanocrystalline magnetic core with high permeability is used, resulting in very high coupling and magnetization inductance. The flux density in this core is determined by the peak value and frequency of the voltage applied across the magnetization inductance. Since a series resonant compensation is employed, the voltage across the magnetization inductance is approximately equal to u_1. This is because the compensation cancels out the voltage drop across the stray inductance, and the voltage drop across the winding resistance—typically in the milliohm range—can be neglected. As a result, similar to a conventional transformer, the flux density in the core depends only on the applied voltage and remains independent of the load. This is evident in (14), where the core losses are influenced solely by the input voltage (its amplitude and frequency), the core's geometry, and the number of turns in the winding around the core. To ensure that the WPT system operates with maximum efficiency, a balance between core and copper losses must be achieved by appropriately selecting the number of turns and the operating frequency. A key limitation in this optimization is the maximum allowable core loss, as excessive losses can lead to an unacceptable rise in core temperature.

In this section, we experimentally determine the precise thermal model of the core using the setup shown in Fig. 7(a). The core is excited with a voltage u_1, which induces a magnetization current i_{m} responsible for generating core losses P_{core}. The core losses are measured using a HIOKI PW8001 power analyzer, which features automatic phase correction for connected current sensors, enabling precise power measurements at low power factors up to the 100 kHz frequency range [16].

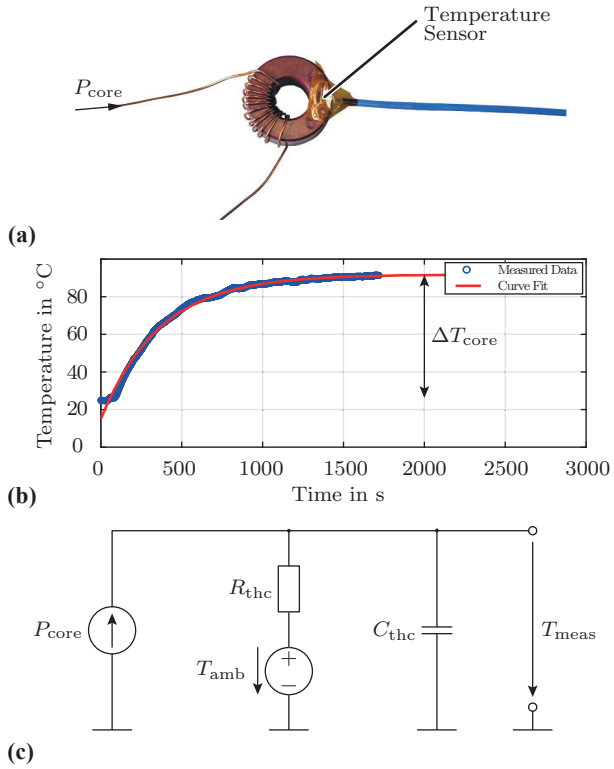

FIGURE 7: Core temperature measurement: (a) The measurement setup is demonstrated. (b) Temperature measurement results with curve fit. (c) Thermal equivalent circuit used for the curve fit.

As a result of the losses P_{core}, the core temperature rises, which is measured using a K-type temperature probe [17]. The sensor is mounted directly onto the core, with the plastic core enclosure removed to establish direct contact with the nanocrystalline core using thermal paste. The measured temperature rise is presented in Fig. 7(b). This thermal behavior is modeled using the thermal circuit network depicted in Fig. 7(c), where the most critical parameter is the thermal resistance of the core, R_{thc}, which is determined from the steady-state temperature rise and core losses as:

$$R_{\text{thc}} = \frac{\Delta T_{\text{core}}}{P_{\text{core}}} = \frac{66.9\,^{\circ}\text{C}}{1.9\,\text{W}} = 35.4 \pm 3\,^{\circ}\text{C}\,\text{W}^{-1}. \quad (16)$$

Where $\pm 3\,^{\circ}\text{C}\,\text{W}^{-1}$ represents the propagated measurement error, which arises from the temperature measurement uncertainty of $\pm 2.4\,^{\circ}\text{C}$ and the power measurement uncertainty of $\pm 0.147\,\text{W}$. For further calculations the "worst case" thermal resistance of $R_{\text{thc}} = 38.4\,^{\circ}\text{C}\,\text{W}^{-1}$ is assumed. The thermal capacitance is particularly useful in scenarios where core losses fluctuate (e.g., due to on/off operation), as it helps predict the rate of temperature increase. The thermal capacitance is estimated using a curve-fitting approach:

$$T_{\text{meas}}(t) = T_{\text{amb}} + P_{\text{core}} R_{\text{thc}} \left(1 - e^{-\frac{t}{R_{\text{thc}} C_{\text{thc}}}}\right), \quad (17)$$

where the optimal thermal capacitance $C_{\text{thc}} = 9.51\,\text{J}\,^{\circ}\text{C}^{-1}$ is determined based on the best fit to the experimental data in Fig. 7(b).

G. WPT Design Optimization

Once all models for the WPT system are established, we can perform an optimization to determine the parameters that result in the highest efficiency. For this WPT system, the input voltage level is fixed ($U_{\text{in}} = 50\,\text{V}$), and the system must deliver $P_{\text{out}} = 200\,\text{W}$ of continuous power. Due to geometric constraints, the nanocrystalline VITROPERM 500 F core (L2020-W409) is selected [18].

The primary parameters for optimization are the number of turns for the primary and secondary windings, which are kept equal ($N_1 = N_2$), and the switching frequency f_{SW}. These parameters are swept over a predefined range with specified steps, as detailed in Tab. 2. The efficiency is calculated for each design, ensuring that all designs remain within the established constraints. The equivalent load resistance R_{eq} is calculated using (8).

The radius of the primary winding, $r_{\text{w1}} = 0.28\,\text{mm}$, was chosen based on the skin depth δ of the expected frequency range. For copper at a frequency of $29\,\text{kHz}$, the skin depth is approximately $\delta \approx 0.38\,\text{mm}$. The copper foil thickness, $b = 0.1\,\text{mm}$, was selected according to the recommendations in [19], which suggest an optimal ratio between foil thickness and skin depth of $X = b/\delta \approx 1/3$. The foil width, $w = 5\,\text{mm}$, was determined by the space constraints imposed by the core: $d_{\text{lim}} = 6\,\text{mm}$. Additionally, core losses are limited to $P_{\text{core}} < (T_{\text{c,max}} - T_{\text{amb}})/R_{\text{th,c}} = 0.95\,\text{W}$.

Finally, all designs are evaluated for power levels below the nominal value, as depicted in Fig. 8. The chosen design is highlighted in the figure, and its parameters are listed in Tab. 2. It is important to note that all designs shown in Fig. 8 satisfy the assumed constraints, while those outside the limitations were discarded.

III. Wireless Data Transmission

Several methods exist to ensure data transmission in WPDT systems. A commonly used approach involves modulating a high-frequency data signal onto the power signal. However, this technique suffers from interference between the data and power signals, [20], where the reached transmission speeds are around $600\,\text{kbit}\,\text{s}^{-1}$. Another option is the use of radio frequency (RF) technologies. Despite their versatility, RF-based solutions have significant drawbacks, including transmission delays of up to several milliseconds [21]. Moreover, since radio frequencies can penetrate opaque materials, they may lead to interference between different joints in the system [22].

Therefore, to address these limitations, the data transfer system described here employs infrared light for communication, where the transceiver and receiver sides are illustrated in Fig. 9. Optical communication allows for separate power and data transmission channels, eliminating interference be-

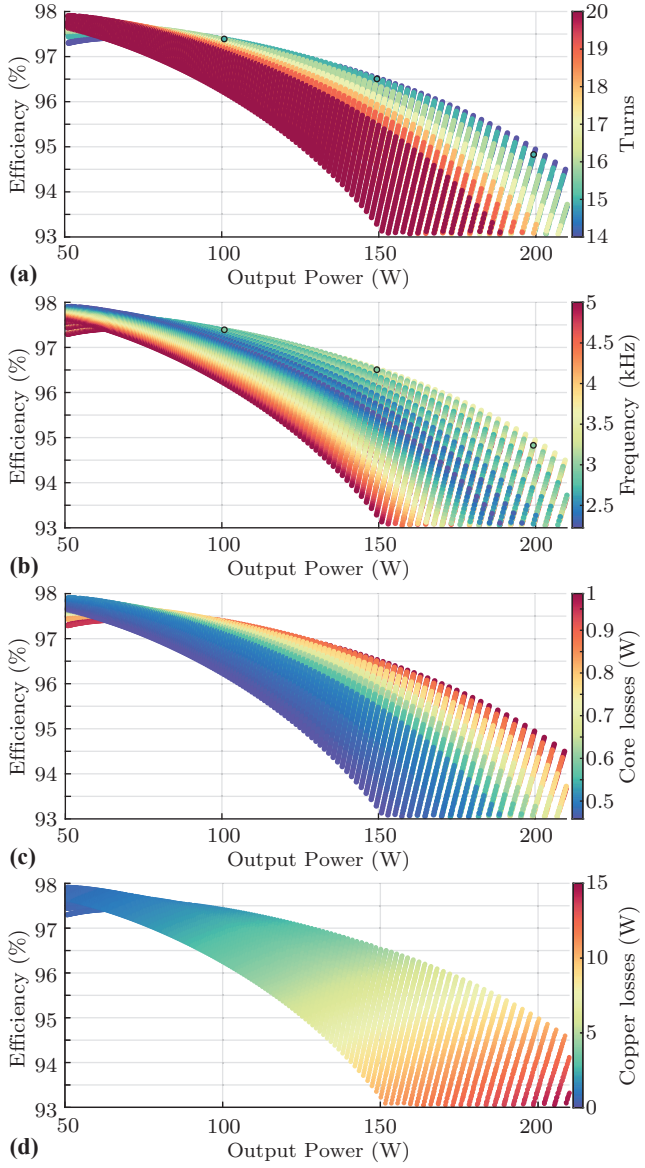

FIGURE 8: Optimization results: System efficiency over output power and the dependency of the number of turns (a) and switching frequency (b). (c) Demonstrates core losses for different configurations and (d) the copper losses.

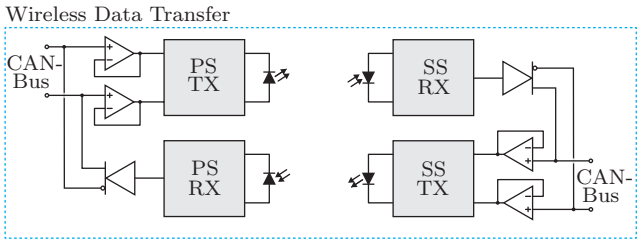

FIGURE 9: Concept of the wireless data transfer using infrared LED's and photodiodes.

TABLE 2: WPT Optimization Parameters.

Parameter	Symbol	Value/Range	Sweep Step
Swept Parameters			
Number of turns	N_1,N_2	$8-20$	1
Switching frequency	f_{sw}	$20-50\,\mathrm{kHz}$	$1\,\mathrm{kHz}$
Fixed Parameters			
Input voltage	U_{in}	$50\,\mathrm{V}$	
Output power	P_{out}	$200\,\mathrm{W}$	
Equivalent load resistor	R_{eq}	$10.13\,\Omega$	
Wire diameter	d_{w1}	$0.56\,\mathrm{mm}$	
Wire length per turn	$l_{\mathrm{w},1}$	$4.4\,\mathrm{cm}$	
Foil winding diameter	d_{w2}	$88\,\mathrm{mm}$	
Foil width	w	$5\,\mathrm{mm}$	
Foil thickness	b	$0.1\,\mathrm{mm}$	
Core size and type		L2020-W409	
Limitations			
Foil winding lim.	d_{lim}	$6\,\mathrm{mm}$	
Ambient temp.	T_{amb}	$22\,^{\circ}\mathrm{C}$	
Max. winding temp.	$T_{\mathrm{w1,max}}$	$190\,^{\circ}\mathrm{C}$	
Max. winding temp.	$T_{\mathrm{w2,max}}$	$60\,^{\circ}\mathrm{C}$	
Max. core temp.	$T_{\mathrm{c,max}}$	$60\,^{\circ}\mathrm{C}$	
Max. peak flux density	B_{sat}	$1.2\,\mathrm{T}$	
Opt. Results			
Number of turns	N_1,N_2	15	
Switching frequency	f_{sw}	$29\,\mathrm{kHz}$	

tween the two signals. Infrared light, particularly in the wavelength range of approximately $900\,\mathrm{nm}$, is a commonly used choice for data transmission due to its cost efficiency, wide availability, and low power requirements [23]. The communication protocol implemented in this system is CAN-Bus, widely used in industrial applications for its robustness and resistance to noise in challenging environments. These features align with the requirements of robotic systems, including robotic dogs, and have been used in such systems [1]. A similar approach for transmitting a CAN-Bus signal using visible light, achieving transmission speeds of up to $200\,\mathrm{kbit\,s^{-1}}$, is demonstrated in [8].

Due to the specific voltage levels of the CAN bus and the required low latency, the circuit shown in Figure 10 was developed. This circuit enables the transmission of CAN-Bus signals between the primary and secondary sides, supporting bidirectional, half-duplex communication. Both sides of the circuit are identical, ensuring symmetry in signal processing. The input to the circuit consist of a differential CAN-Bus signal, composed of the CAN-High and CAN-Low lines. The voltage level on the CAN-High line varies between $2.5\,\mathrm{V}$ and $3.5\,\mathrm{V}$, while the voltage on the CAN-Low line ranges from $1.5\,\mathrm{V}$ to $2.5\,\mathrm{V}$, depending on whether a logical one or zero is transmitted. The data transmission circuit can be divided into three parts: the transmitter circuit, the receiver circuit, and the decoupling circuit, which is highlighted in grey in

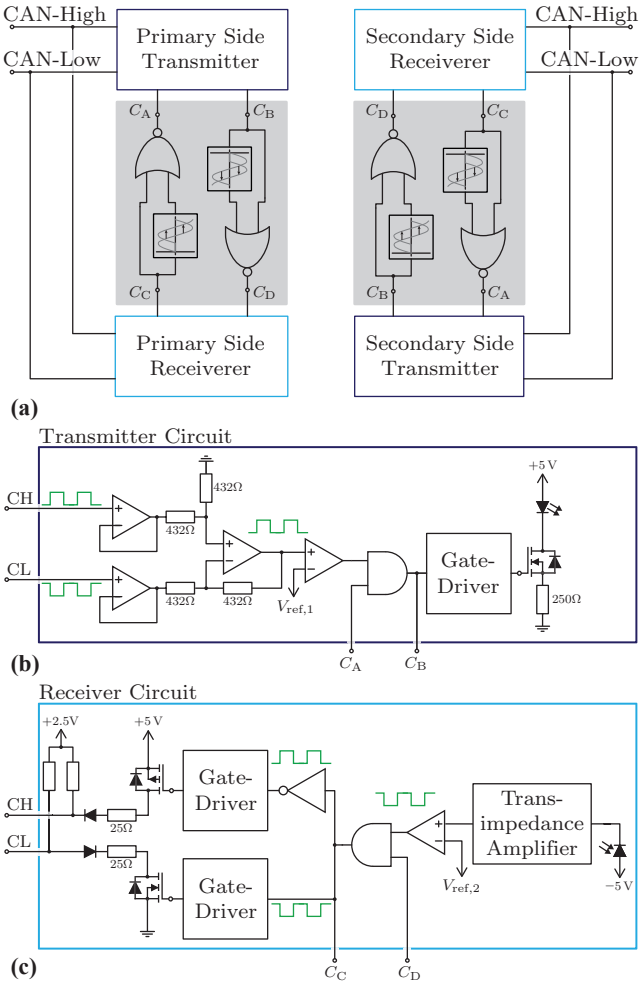

FIGURE 10: The structure of the data transmission circuit is shown: (a) Data transmission circuit primary and secondary side connected with a decoupling circuit. (b) Transmitter Circuit. (c) Receiver circuit.

Fig. 10(a). These circuits will be explained in detail in the following sections.

A. Transmitter Circuit

In Fig. 10(b), the transmitter circuit is shown. This circuit receives the CAN-Bus signal (depicted in green) as input, which is first processed by two voltage follower circuits. These voltage followers have a high input impedance, minimizing the circuit's influence on the CAN-Bus. The differential CAN-Bus signal is then converted into a single-ended signal using a subtractor circuit, which subtracts the CAN-Low signal from the CAN-High signal. Since the voltage levels on the CAN-Bus may fluctuate, the single-ended signal is compared to a reference voltage $V_{\mathrm{ref},1}$ using a comparator, which converts it into a binary signal of $0\,\mathrm{V}$ or $3.3\,\mathrm{V}$. This signal is then passed through an AND gate (which will be explained later when the decoupling circuit is discussed) to a gate driver, which controls an N-channel MOSFET. This MOSFET is used to turn the current through the LED on and off. The light emitted by the LED is used as the medium for wireless data transmission.

B. Receiver Circuit

Fig. 10(c) illustrates the receiver circuit. The light signal emitted by the LED is detected by a photodiode, which converts it into a current proportional to the incoming light intensity. A negative bias voltage of $-5\,\mathrm{V}$ is applied to the photodiode to reduce the junction capacitance, allowing for faster rise and fall times. The current generated by the photodiode is then converted into a voltage signal using a transimpedance amplifier [24] and subsequently processed by a comparator to ensure well-defined voltage levels. This step is necessary because the photodiode always produces a small current (dark current), meaning the output of the transimpendace amplifier is always above $0\,\mathrm{V}$. Additionally, the light intensity fluctuates depending on the position of the joint due to changes in the relative position between the LED and photodiode. The single-ended output signal from the comparator is passed through an other AND-Gate (which again will be referenced later) and then converted into a differential signal using an inverting gate. This differential signal is then used to control two MOSFETs. Using a combination of an N-channel and a P-channel MOSFET, the differential signal is applied to the CAN-Bus lines. The P-channel MOSFET connects the CAN-High line to $5\,\mathrm{V}$ when activated, and the N-channel MOSFET connects the CAN-Low line to $0\,\mathrm{V}$ when activated. Since these voltage levels do not match the CAN-Bus standard levels of $3.5\,\mathrm{V}$ and $1.5\,\mathrm{V}$, two resistors are added in series with the CAN-Bus line to adjust the voltage. The values of these resistors are chosen so that the voltage drop across them exactly compensates for the difference in voltage. This approach was chosen to reduce the number of voltage regulators on the PCB. Additionally, two diodes are connected in series with the CAN-Bus lines: The diode on the CAN-High line prevents current from flowing into the $5\,\mathrm{V}$ supply if the CAN-Bus voltage exceeds $5\,\mathrm{V}$. The diode on the CAN-Low line prevents current flow from the ground to the CAN-Low line if the CAN-Low voltage drops below $0\,\mathrm{V}$. If one or both switches are open, the respective CAN line is passively pulled to $2.5\,\mathrm{V}$ with a resistor connected between the CAN line and the $2.5\,\mathrm{V}$ supply voltage.

C. Decoupling Circuit

Decoupling the transmitters and receivers on both primary and secondary sides is crucial for two significant reasons. First, a potential deadlock scenario exists through the CAN-Bus as follows: When a dominant state appears at the primary side transmitter circuit input, this signal propagates to the secondary side receiver, fixing the secondary CAN-Bus state. Subsequently, the secondary side transmitter relays this state back to the primary side receiver, resulting in a

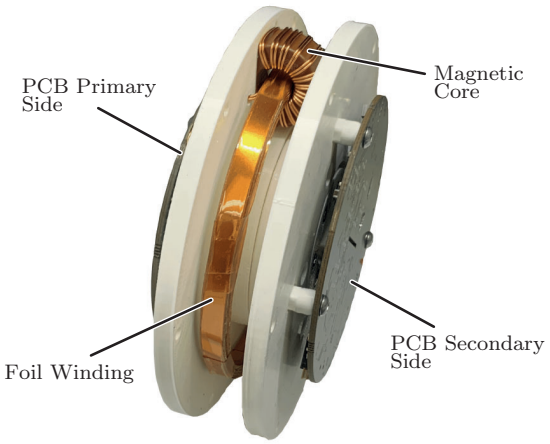

FIGURE 11: Hardware demonstrator of the WPDT system for the robotic joint used to validate theoretical results.

persistent dominant state lock condition. Second, unintended receiver detection operations can occur due to the proximity of LED placement. These operational anomalies can be effectively avoided by implementing decoupling circuits as illustrated in Fig. 10(a).

The transmitter and the receiver are connected to each other at the points C_{A}, C_{B}, C_{C} and C_{D}. The points C_{A} and C_{D} are linked to the previously mentioned AND gates in the transmitter and receiver circuits. To prevent false detections, a decoupling circuit between points C_{B} and C_{D} is implemented. This circuit, in combination with the AND gate in the receiver circuit, disables the receiver when the LED on the same side is turned on. The functionality is as follows:

- When the LED is on (C_{B} = HIGH), the NOR gate drives the signal to LOW, which forces the output of the AND gate in the receiver circuit to LOW, regardless of the transimpedance amplifier's output. A LOW output from the AND gate prevents the receiver circuit from influencing the CAN-Bus state.
- When the LED is off (C_{B} = LOW), the NOR gate drives the signal to HIGH, which means that the output of the AND gate corresponds to the output of the transimpedance amplifier.

Additionally, a delay block at one input of the NOR gate extends the receiver circuit's deactivation time, compensating for propagation delays in the circuit.

To prevent the deadlock scenario, the same decoupling circuit is applied between points C_{C} and C_{A}. Here, the transmitter is always disabled when the signal at point C_{C} is HIGH. This prevents a received signal from being transmitted back to the other side, eliminating the risk of a persistant dominant state lock condition.

TABLE 3: Hardware Demonstrator Parameters for $f_{\mathrm{SW}} = 29\,\mathrm{kHz}$, $N = 15$ and $P_{\mathrm{out}} = 200\,\mathrm{W}$

Parameter	Symbol	Value
Mutual inductance	L_{m}	12.2 mH
Stray inductance primary side	L_{s1}	2.3945 µH
Stray inductance secondary side	L_{s2}	36.283 µH
Winding resistance primary side	R_{w1}	24.6 mΩ
Winding resistance secondary side	R_{w2}	445 mΩ
Primary winding length	l_{w1}	4.4 cm
Primary winding radius	r_{w1}	0.28 mm
Secondary winding width	w	5 mm
Secondary winding height	h	0.1 mm
Secondary winding diameter	d_{w2}	88 mm
Number of turns	N	15
Coupling coefficient	k	0.998
Weight (PCB's + core + windings)	m	96 g

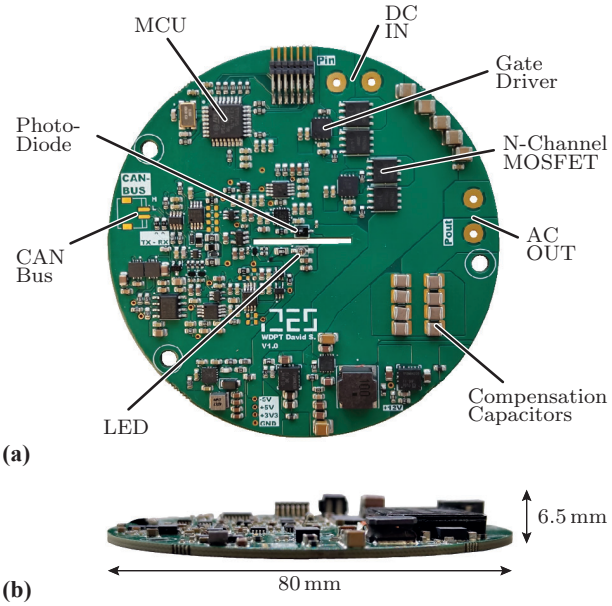

FIGURE 12: The prototype of the proposed WPDT system: (a) Primary side PCB with full-bridge inverter and data transmission circuit. (b) PCB sideview showing the thickness of 6.5 mm.

IV. Hardware Implementation and Experiments Results

A. Wireless Power Transfer

To validate the theoretical and design results of the WPDT system for robotic joints, a hardware demonstrator based on the optimized design from Fig. 8 was built. The demonstrator is shown in Fig. 11. The demonstrator parameters are given in Tab. 3. It is designed to emulate a robotic joint that can rotate, supported by mechanical ball bearings. The supporting assembly for the core, along with the primary winding that rotates around the secondary foil winding, is constructed from 3D-printed material. Two PCBs are mounted on the axial sides of the demonstrator assembly. The primary side PCB is supplied with $50\,\mathrm{V_{dc}}$, driving the primary winding via a full-bridge converter. The primary PCB rotates together with the primary core and winding. Meanwhile, the secondary PCB is fixed to the secondary foil winding, rectifying the received voltage and current to deliver a DC output on the secondary side.

The maximum possible rotation angle is $\alpha = 310°$. Communication between the primary and secondary PCBs is integrated and achieved optically through the center of the joint, which is kept free for this purpose, as shown in Fig. 1.

A detailed view of the PCB is provided in Fig. 12. For the primary side (see Fig. 12 (a)), the full-bridge inverter is implemented using two *Texas Instruments* half-bridge drivers [25] in combination with external N-channel MOSFETs. The two half-bridges are connected in parallel to form a full-bridge configuration.

To compensate for the primary stray inductance (see Tab. 3 for values), a series compensation capacitance C_{s1} (refer to Fig. 2 for the schematic) is realized using ceramic capacitors with a C0G dielectric. This ensures that the capacitance remains stable and unaffected by voltage bias, maintaining accurate resonance compensation. The primary stray inductance is relatively low ($L_{\mathrm{s1}} = 2.4\,\mu\mathrm{H}$) due to the tightly wound primary winding around the toroidal core. However, compensating for this low inductance requires a large value for the compensation capacitance, which would necessitate an impractical number of capacitors connected in parallel. To address this, the total compensation capacitance $C_{\mathrm{tot}} = C_{\mathrm{s1}} + C_{\mathrm{s2}}$ is distributed between the primary and secondary side PCBs, thereby reducing the overall number of capacitors required. When calculating the compensation capacitors, the following condition must be satisfied - under the assumption $i_{\mathrm{m}} \approx 0$:

$$\frac{1}{C_{\mathrm{s1}}} + \frac{1}{C_{\mathrm{s2}}} = \left(2\pi f_{\mathrm{SW}}\right)^2 \cdot \left(L_{\mathrm{s1}} + L_{\mathrm{s2}}\right).$$

This capacitance is realized by connecting $16 \times 0.15\,\mu\mathrm{F}$ ceramic capacitors in parallel on the primary side, and $8 \times 0.15\,\mu\mathrm{F}$ on the secondary side [26].

The secondary side PCB is equipped with a rectifier that utilizes the Active Rectifier Controller *LT4322* from *Analog Devices* [27]. This controller ensures that the external N-channel MOSFET is switched on or off based on the diode conduction state, effectively eliminating diode forward voltage drop losses. The total weight of the system, including the PCBs, the primary and secondary coils, and the magnetic core, is $96\,\mathrm{g}$.

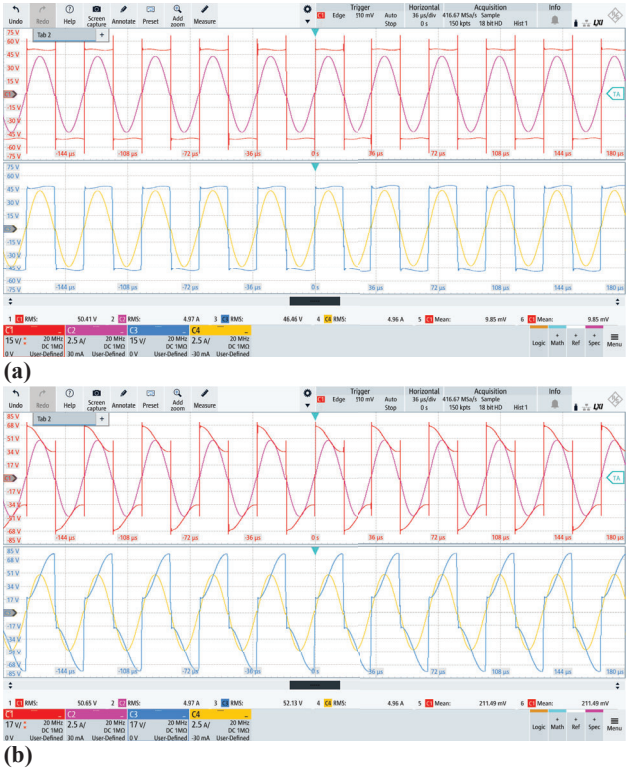

(a)

(b)

FIGURE 13: Results of power efficiency measurement: (a) Primary side voltage and current (top) and secondary side voltage and current (bottom) measured at the full-bridge output and rectifier input. (b) Voltage and current waveforms measured at the transformer input and output.

The first step in the experimental verification is to ensure that the resonant compensation functions as intended, i.e., that sinusoidal current, in phase with the pulsed voltage, is achieved for both the primary and secondary sides, including the rectifier. These measurements are shown in Fig. 13(a), where the upper plot displays the primary side (blue) and the lower plot displays the secondary side (red). The operating frequency is $29\,\mathrm{kHz}$, and for the waveforms shown, the resulting current peak is $7.4\,\mathrm{A}$.

The first efficiency measurement focuses on the efficiency of the *transformer part* only to validate the loss models from Sec. II. Due to voltage compensation, the voltage across the transformer is not pulsed, as depicted in Fig. 13(b). The input and output power at different power levels were also measured using the power analyzer. These values allow us to calculate the transformer losses (including winding and core losses) and the resulting efficiency, which is presented in Fig. 14.

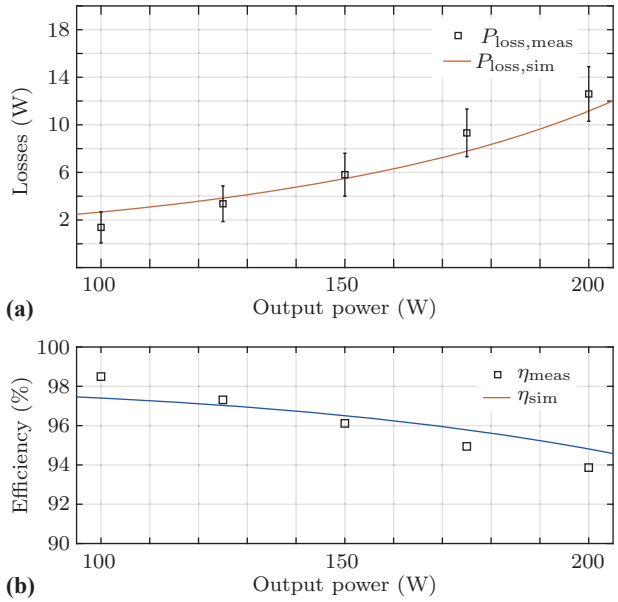

FIGURE 14: Transformer loss measurement: (a) Total loss measurement and simulation result over the output power. The vertical line over the measurement point denotes the measurement error range. (b) Simulated and measured efficiency over the output power.

In the same plots, theoretical results based on the loss models derived in Sec. II are represented with solid lines, while measurement results are shown as squares. Vertical lines around each measurement point indicate the estimated measurement error, accounting for the accuracy of the measurement equipment. The results demonstrate that the model predicts losses well and within the measurement error boundaries.

It is also evident that efficiency decreases with increasing output power. This trend is primarily due to the dominant winding losses in the system (see Fig. 8(c-d)), which are attributed to the long secondary winding. This extended winding is geometrically necessary to allow the primary core to rotate around it.

Finally, when the entire system is operated, including both power and data transfer, and all power consumption from the PCB components is accounted for—such as the power supplying the data transfer components, the power transfer control electronics, the resonant capacitors, and the transformer—the system achieves a DC-to-DC efficiency of $90.3\,\%$ at $200\,\mathrm{W}$, as shown in the measurements in Fig. 15. The losses caused by the data transmission circuitry depend on the data transmission speed. For the target transmission speed of $2\,\mathrm{Mbit\,s^{-1}}$, these losses amount to approximately $6\,\mathrm{W}$. If the power consumption of the communication circuitry is excluded, the efficiency improves to $93\,\%$. For lower power levels, the efficiency increases since the main loss component in the power transfer system stems from

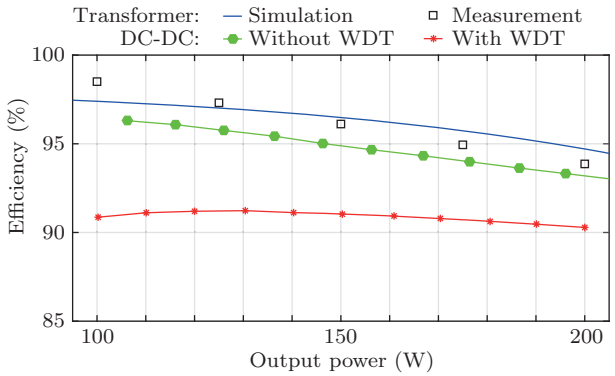

FIGURE 15: Comparison between simulated transformer efficiency, measured transformer efficiency and measured DC-DC efficiency with and without data transfere.

copper losses in the secondary foil winding. For instance, at $100\,\mathrm{W}$ of power transmission, the DC-to-DC efficiency rises to $90.9\,\%$ with WDT and to approximately to $96.5\,\%$ without WDT (see Fig. 15 for reference). As seen in Fig. 14(b), the efficiency of the 'transformer part' alone exceeds $94\,\%$ at an output power of $200\,\mathrm{W}$. However, because the power level transferred is relatively low, the power consumption of auxiliary circuits and components on the PCB significantly impacts the overall DC-to-DC efficiency of the WPDT system.

B. Wireless Data Transfer

The PCBs shown in Fig. 11 both implement the transmitter and receiver circuits described in Section III. Additionally, each PCB features a CAN-Bus transceiver, which handles the level conversion between the differential signal of the CAN-Bus and the logical signal level required by the CAN controller integrated into the MCU. The CAN-High and CAN-Low pins of the transceiver are connected to the inputs of the data circuit showed in Fig. 10, facilitating the bidirectional wireless transmission of signals between the primary and secondary sides. The maximum achievable data transmission rate is influenced not only by the rise and fall times of the WDT circuit, but also by its propagation delay. This is due to the fundamental operating principle of the CAN-Bus: when a message is sent, the receiver acknowledges successful reception with an ACK bit. If the sender does not receive this ACK bit within a specific time frame, an error is triggered. The length of this time frame depends on the transmission speed.

To achieve high data transmission rates, components with low rise and fall times as well as minimal propagation delay, like [28], were selected. To verify the data transmission functionality, an isolated test was conducted, during which no power was transmitted. In this test, the CAN-Bus transceiver on the primary side generated a CAN signal, which was transmitted to the secondary side via the WDT circuit. The

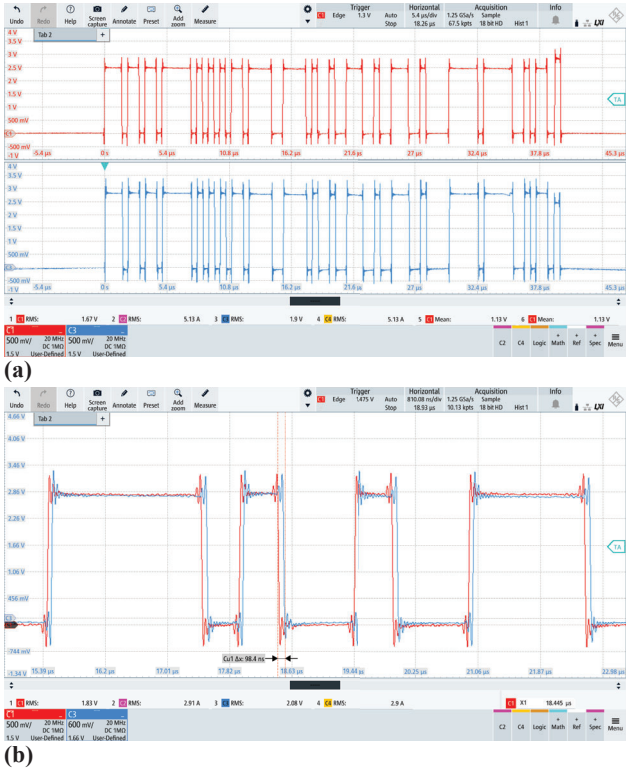

(a)

(b)

FIGURE 16: Result of the data transmission measurement: (a) Data signal primary and secondary side. (b) Data signal transmission delay.

CAN-Bus transceiver on the secondary side received the signal and passed it on to the MCU.

The measurement results are shown in Fig. 16, where a maximum data transmission rate of $2\,\mathrm{Mbit\,s^{-1}}$ was achieved. Fig. 16(a) illustrates the voltage difference between the CAN-High and CAN-Low lines. The red signal represents the CAN signal generated on the primary side, while the blue signal corresponds to the CAN signal received on the secondary side and transmitted via the WDT circuit. Fig. 16(b) depicts the propagation delay occurring during transmission between the primary and secondary sides, which amounts to $100\,\mathrm{ns}$. This propagation delay is the limiting factor for the maximum achievable data transmission rate of $2\,\mathrm{Mbit\,s^{-1}}$.

C. Wireless Power and Data Transfer

In the previous sections, successful data and power transmission were demonstrated. However, the simultaneous transmission of power and data needs to be verified. As in the previous measurements, an output power of $200\,\mathrm{W}$ and a data transmission rate of $2\,\mathrm{Mbit\,s^{-1}}$ are used for the experiment. The measurement results are shown in Fig. 17. The upper half of the figure displays the currents on the primary and secondary sides of the transformer, while the lower half shows the differential voltage between the CAN-High and CAN-Low lines on both the primary and secondary sides.

TABLE 4: Comparison between WPDT systems using different approaches

Reference	$P_{out}[\mathrm{W}]$	$\eta[\%]$	Data rate $[\mathrm{kbit\,s^{-1}}]$	Com. Mode
This work	200	93	2000	Half-duplex
[29]	500	86	20	Full-duplex
[30]	180	90	19.2	Half-duplex
[31]	300	90.1	500	Full-duplex
[6]	50	-	1700	Full-duplex
[20]	500	84	600	Full-duplex
[32]	100	84	200	Full-duplex

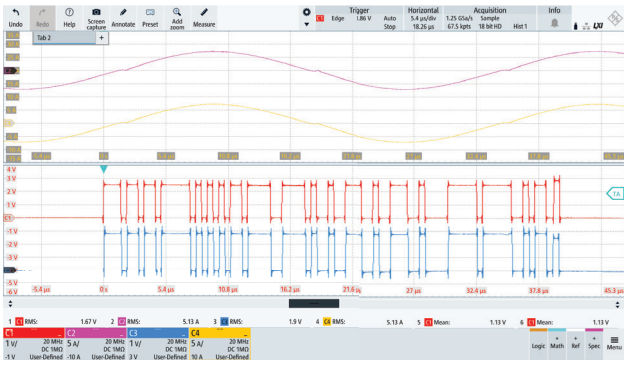

FIGURE 17: Simultaneously power and data transfer: In the upper half of the image, the currents on the primary and secondary sides were measured, while in the lower half of the image, the CAN bus signal on the primary and secondary sides was measured.

Thus, a successful simultaneous data and power transfer can be confirmed. Furthermore, no impact of power transmission on the data transmission was observed. Compared to the WPDT systems presented in Table 4, a significant improvement in both data rate and power transfer efficiency was achieved. The reported DC-to-DC efficiency is explicitly provided in Table 4, whereas in other publications, it is not always clearly specified whether the reported efficiencies refer to DC-to-DC efficiency or only transformer efficiency. The latter is typically higher, as seen in our WPT system, where the transformer efficiency reaches $94\,\%$ at $200\,\mathrm{W}$.

D. Transient Behaviour

In robotic joints, particularly those used in quadruped robots, load spikes frequently occur, leading to a sudden increase in the required output power. Fig. 18 illustrates the system behavior during such a load spike, where the output power rises abruptly from approximately $50\,\mathrm{W}$ to around $300\,\mathrm{W}$. This change in output power was induced by manually connecting an additional resistor in parallel to the load resistance.

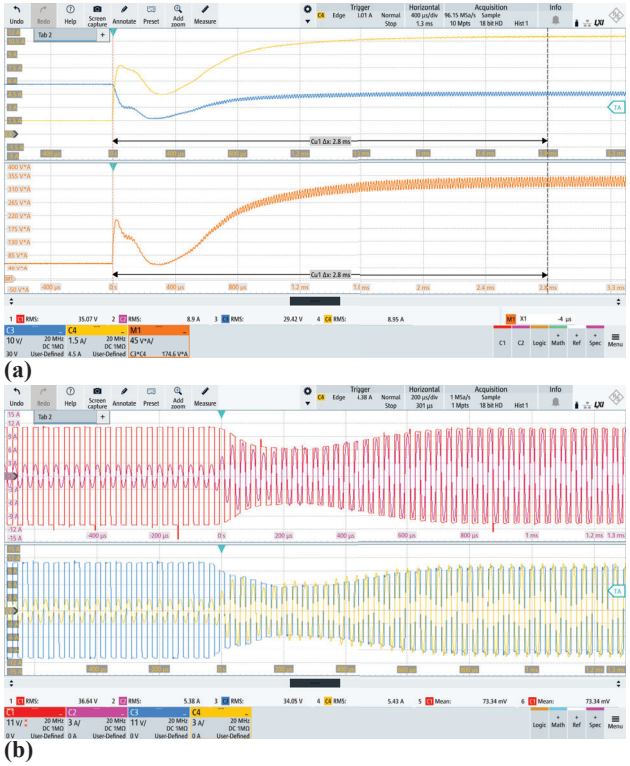

(a)

(b)

FIGURE 18: Step response of the system in output power from 50 W to 300 W: (a) DC output voltage U_{out} and output current. (b) Measured voltage and current waveforms on the primary side (top) and secondary side (bottom) are shown.

Fig. 18(a) presents the output voltage and current waveforms (top), as well as the corresponding output power (bottom). Fig. 18(b) depicts the voltage and current waveforms on both the primary and the secondary side of the transformer. The measurement results confirm that the system can effectively handle such load transients while maintaining a sinusoidal current waveform. It should be noted that the high output power results in a significant increase in current, which in turn leads to a greater voltage drop across the winding resistances. This effect can be observed in Fig. 18(a). Further investigation into the transient behavior of the system should be carried out.

V. Conclusion

This paper presents a novel approach to wireless power transfer (WPT) for robotic joints, utilizing a closed magnetic core to couple the primary and secondary windings. Additionally, wireless data transfer (WDT) is integrated with the power transfer, resulting in a comprehensive wireless power and data transfer (WPDT) system for robotic joints. Theoretical models for winding and core losses are derived and employed to optimize the WPT system components, identifying the optimal number of winding turns and the optimal switching frequency for operation. For WDT, photodiodes are utilized, and custom-designed electronic circuits employing low-latency operational amplifiers and MOSFETs ensure minimal delay of 100 ns in handling CAN bus signals.

The WPDT system is validated experimentally using a custom-built hardware demonstrator, achieving 200 W power transfer with 94 % transformer efficiency and 93 % DC-to-DC efficiency. Additionally, a data transfer speed of up to $2\,\mathrm{Mbit\,s^{-1}}$ is demonstrated. The results are compared to existing literature and discussed in detail.

Future work will focus on reducing AC losses in the foil winding by introducing magnetic shielding, minimizing the power consumption of electronic circuits, and evaluating magnetic field emissions to ensure compliance with relevant guidelines for limiting exposure to time-varying electric, magnetic, and electromagnetic fields.

ACKNOWLEDGMENT

The authors gratefully acknowledge the financial support provided by UIBK's 1669 Prototypenentwicklung funding for this project.

REFERENCES

[1] B. Katz, J. D. Carlo, and S. Kim, "Mini cheetah: A platform for pushing the limits of dynamic quadruped control," in *2019 International Conference on Robotics and Automation (ICRA)*, 2019, pp. 6295–6301.

[2] M. Hutter, C. Gehring, D. Jud, A. Lauber, C. D. Bellicoso, V. Tsounis, J. Hwangbo, K. Bodie, P. Fankhauser, M. Bloesch, R. Diethelm, S. Bachmann, A. Melzer, and M. Hoepflinger, "Anymal - a highly mobile and dynamic quadrupedal robot," in *2016 IEEE/RSJ International Conference on Intelligent Robots and Systems (IROS)*, 2016, pp. 38–44.

[3] X. Li, G. Zhu, M. Pang, K. Xiang, J. Lu, and W. Yue, "Analysis and design of wireless power transfer system for robot joints," in *2022 IEEE 5th International Electrical and Energy Conference (CIEEC)*, 2022, pp. 1826–1830.

[4] A. Esser and H.-C. Skudelny, "A new approach to power supplies for robots," *IEEE Transactions on Industry Applications*, vol. 27, no. 5, pp. 872–875, 1991.

[5] S. Kikuchi, T. Sakata, E. Takahashi, and H. Kanno, "Development of wireless power transfer system for robot arm with rotary and linear movement," in *2016 IEEE International Conference on Advanced Intelligent Mechatronics (AIM)*, 2016, pp. 1616–1621.

[6] K. Serizawa, S. Shimizu, H. Sekiya, and M. Ohira, "Development of robotic system without wired connections at joints by wireless communication and wireless power transfer," in *2022 IEEE 33rd Annual International Symposium on Personal, Indoor and Mobile Radio Communications (PIMRC)*, 2022, pp. 01–07.

[7] S. Mirić, J. Xu, J. Huber, D. Bortis, M. Hitz, and J. W. Kolar, "Wireless power supply of moving linear actuator enclosed in stainless-steel," in *2022 Wireless Power Week (WPW)*. IEEE, 2022, pp. 354–360.

[8] K.-R. Sohn, H.-J. Lee, and Y.-J. Kim, "Wireless can communications based on white led," in *2011 Third International Conference on Ubiquitous and Future Networks (ICUFN)*, 2011, pp. 127–130.

[9] M. Rozman, K. M. Rabie, and B. Adebisi, "Wireless power and communication transmission for industrial robots," in *2018 11th International Symposium on Communication Systems, Networks & Digital Signal Processing (CSNDSP)*, 2018, pp. 1–5.

[10] J. E. Huber, J. Miniböck, and J. W. Kolar, "Generic derivation of dynamic model for half-cycle dcm series resonant converters," *IEEE Transactions on Power Electronics*, vol. 33, no. 1, pp. 4–7, 2017.

[11] R. Bosshard, "Multi-objective optimization of inductive power transfer systems for ev charging," Doctoral Thesis, ETH Zurich, Zurich, 2015.

[12] O. M. Knecht, "Transcutaneous energy and information transfer for left ventricular assist devices," Doctoral Thesis, ETH Zurich, Zurich, 2017.

[13] K. Xia, B. Zhu, Y. Lou, and D. Huang, "A rotary wireless power transfer system with rail-type coupling structure," *IEEE Access*, vol. 12, pp. 63 967–63 975, 2024.
[14] J. Mühlethaler, "Modeling and multi-objective optimization of inductive power components," Doctoral Thesis, ETH Zurich, Zurich, 2012.
[15] Ansys, Inc., *Ansys Electromagnetics Suite, Release 2024, Help System*, 2024, available: https://www.ansys.com.
[16] K. Hayshi, "Real operating loss measurement of low-loss inductors using high-precision wideband power analyzer and current sensor," Online, 2021. [Online]. Available: https://www.hioki.com/download/38355
[17] Brymen, "Bkp60 k-type temperature probe," Online, 2025, k-type temperature probe, operating range: -20°C to 250°C. [Online]. Available: https://www.brymen.com
[18] V. G. . C. KG, "Datasheet: T60006-l2020-w409-09," https://www.vacuumschmelze.com, November 2019, core material: VITROPERM 500 F, Toroidal core for common mode choke applications.
[19] F. Zach, *Leistungselektronik: Ein Handbuch Band 1 / Band 2*, 6th ed. Springer Vieweg Wiesbaden, 2022, published as part of the Computer Science and Engineering (German Language) eBook package. Hardcover due: 05 July 2022. eBook published: 30 March 2022. [Online]. Available: https://doi.org/10.1007/978-3-658-31436-1
[20] P. Wang, Y. Sun, Y. Feng, T. Feng, Y. Fan, and X. Li, "An improvement of snr for simultaneous wireless power and data transfer system with full-duplex communication mode," *IEEE Transactions on Power Electronics*, vol. 37, no. 2, pp. 2413–2424, 2022.
[21] F. Zheng, J. Xiao, X. Wu, W. Gong, and N. Wu, "A parallel transmission of power and data for ev dynamic wireless charging systems," in *2023 IEEE International Conference on Image Processing and Computer Applications (ICIPCA)*, 2023, pp. 1310–1315.
[22] J. Kahn and J. Barry, "Wireless infrared communications," *Proceedings of the IEEE*, vol. 85, no. 2, pp. 265–298, 1997.
[23] R. Ramirez-Iniguez and R. Green, "Indoor optical wireless communications," in *IEE Colloquium on Optical Wireless Communications (Ref. No. 1999/128)*, 1999, pp. 14/1–14/7.
[24] A. Devices, "Ltc6560 low power transimpedance amplifier," 2019. [Online]. Available: https://www.analog.com
[25] Texas Instruments, "UCC27284 3-A 120-V Half-Bridge Driver with Negative Voltage Handling and Low Switching Losses," https://www.ti.com, 2022, accessed: 2025-04-24.
[26] KEMET, "C1210x154j5gactu - ceramic capacitor, 150nf, 50v, x7r, 1210," https://www.kemet.com/en/us.html, 2025, ceramic C0G capacitors.
[27] Analog Devices, *Floating, High-Voltage Active Rectifier Controller*, 2023.
[28] I. Analog Devices, *AD8000: 1.5 GHz, Ultrahigh Speed Op Amp*, 2016. [Online]. Available: https://www.analog.com
[29] J. Wu, C. Zhao, Z. Lin, J. Du, Y. Hu, and X. He, "Wireless power and data transfer via a common inductive link using frequency division multiplexing," *IEEE Transactions on Industrial Electronics*, vol. 62, no. 12, pp. 7810–7820, 2015.
[30] Y. Li, X. Li, and X. Dai, "A simultaneous wireless power and data transmission method for multi-output wpt systems: Analysis, design, and experimental verification," *IEEE Access*, vol. 8, pp. 206 353–206 359, 2020.
[31] Y. Yao, H. Cheng, Y. Wang, J. Mai, K. Lu, and D. Xu, "An fdm-based simultaneous wireless power and data transfer system functioning with high-rate full-duplex communication," *IEEE Transactions on Industrial Informatics*, vol. 16, no. 10, pp. 6370–6381, 2020.
[32] Y.-G. Su, W. Zhou, A. P. Hu, C.-S. Tang, S.-Y. Xie, and Y. Sun, "Full-duplex communication on the shared channel of a capacitively coupled power transfer system," *IEEE Transactions on Power Electronics*, vol. 32, no. 4, pp. 3229–3239, 2017.